

# Electrically Tunable Flat Bands and Magnetism in Twisted Bilayer Graphene

T. M. R. Wolf, J. L. Lado, G. Blatter, and O. Zilberberg  
*Institute for Theoretical Physics, ETH Zurich, 8093 Zurich, Switzerland*

(Dated: September 4, 2019)

Twisted graphene bilayers provide a versatile platform to engineer metamaterials with novel emergent properties by exploiting the resulting geometric moiré superlattice. Such superlattices are known to host bulk valley currents at tiny angles ( $\alpha \approx 0.3^\circ$ ) and flat bands at magic angles ( $\alpha \approx 1^\circ$ ). We show that tuning the twist angle to  $\alpha^* \approx 0.8^\circ$  generates flat bands away from charge neutrality with a triangular superlattice periodicity. When doped with  $\pm 6$  electrons per moiré cell, these bands are half-filled and electronic interactions produce a symmetry-broken ground state (Stoner instability) with spin-polarized regions that order ferromagnetically. Application of an interlayer electric field breaks inversion symmetry and introduces valley-dependent dispersion that quenches the magnetic order. With these results, we propose a solid-state platform that realizes electrically tunable strong correlations.

Controllably engineering quantum states of matter is one of the leading goals of modern physics. This basic idea has been realized in a plethora of platforms ranging from cold-atom setups [1–3] to atom-by-atom deposited solids [4, 5]. In recent years, the discovery of graphene has opened numerous new avenues [6], including the possibility of stacking two-dimensional crystals and forming so-called ‘van der Waals’ materials [7], which allow to engineer exotic states [7–11]. Tuning the relative angle  $\alpha$  between graphene layers [12] and applying electric potentials  $V$  across the layers [11, 13] have played central roles in purposely designing the physical properties of such systems. In this Letter, we combine these two ideas in a new parameter regime: (i) we identify an angle  $\alpha$  that generates flat bands with strong correlations leading to a magnetic instability, while (ii) an electric bias  $V$  across the layers reintroduces dispersion and thus allows to dynamically tune the magnetic response of the bilayer system.

Stacking graphene layers at a finite relative angle  $\alpha$  produces a moiré superlattice [see Fig. 1(a)] with properties that are sensitive to the twist angle [14–16]. The spectrum of the superlattice is composed of graphene bands that are folded back to the mini-Brillouin zone where they bundle into separate groups; these can be tuned to become flat at small twist angles  $\alpha$ . Such weakly twisted bilayer graphene then provides a versatile platform to explore strongly correlated physics. Much work has focused on the so-called magic angle  $\alpha = 1.1^\circ$  producing two flat bands near charge neutrality (each fourfold degenerate) with strong correlations [9, 17–20] and superconductivity [10, 21, 22] appearing under weak doping. The question arises, whether other angles and bands can be used in engineering novel properties. Here, we show that tuning the twist to the angle  $\alpha^* \approx 0.8^\circ$  flattens the bands above and below the ones near charge neutrality. We find that doping these bands to half-filling with  $\pm 6$  electrons per triangular supercell produces a correlated state with ferromagnetic order.

Such flat bands have been termed ‘pseudo-Landau lev-

els’ (PLLs) [23–25]; they can be understood as the result of artificial gauge fields that arise from nonuniform strain in graphene monolayers [26–28] or twist-induced strain between layers [29]. Proper tuning of such strain leads to hopping phases that interfere destructively, localizing the states and producing flat bands [23, 24]. Similar flat-band modes have been proposed in other twisted multilayer systems [30], such as tiny-angle graphene bilayer [31], graphene trilayers [32], graphene bi-bilayers [33, 34], and dichalcogenide multilayers [35].

An alternative way to engineer the electronic states in multilayers of Dirac materials is to apply an interlayer bias  $V$  to induce valley Berry curvature [13]. The latter results from breaking inversion symmetry, that induces topology through (compensating) valley fluxes [11, 36]. Such valley fluxes and associated valley currents are particularly pronounced at small twist angles and cause dispersive splittings between bands [36]. This motivates the idea of engineering the bandwidth and correlations via electrical bias and geometric twist. Here, we combine twist-induced emergent flat bands at small twist  $\alpha$  and an interlayer bias  $V$  in order to manipulate the strong-correlation physics in a flat-band material with valley-topological properties.

Flat-band magnetism in twisted bilayer graphene has been discussed before with a focus on the bands near charge neutrality and manipulation of the magnetic state by interlayer bias [37–39] and by pressure [39]. Rather than manipulating the 0th PLL near charge degeneracy, we focus on the  $\pm 1$  PLLs that become optimally flat at the smaller angle  $\alpha^* \approx 0.8^\circ$  where valley currents are more pronounced. Different from the 0th PLL bands that are described by an effective honeycomb lattice and flat Dirac cones, the  $\pm 1$  PLLs are described by a triangular lattice. We study the delocalization effect of the bias-induced local valley fluxes and find that these act against the subtle spatial interference that generates the original flat bands. The bias-induced dispersion then reduces the correlations and thus the ferromagnetic (quasi-)order in the material,

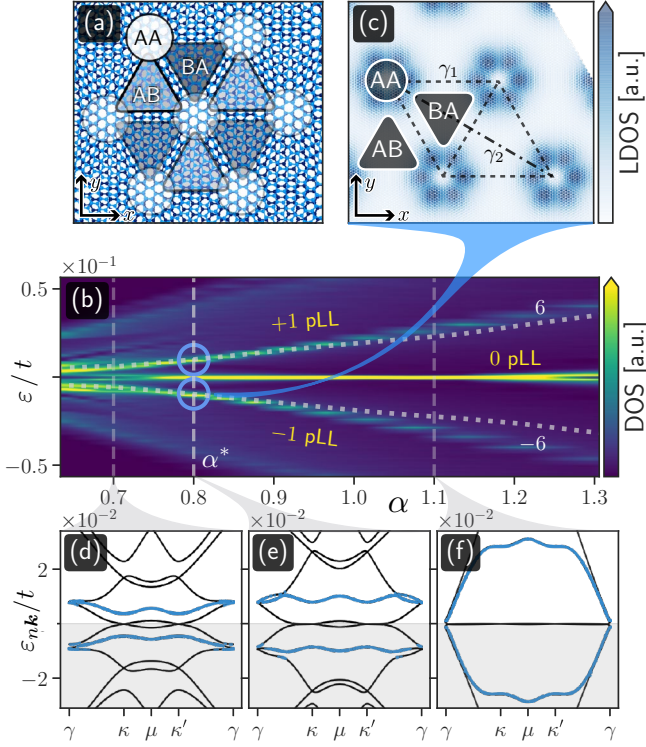


FIG. 1. Tunability of the single-particle bilayer graphene properties as a function of the twist angle. (a) Stacking two honeycomb lattices (light/dark blue) with small twist angle  $\alpha$  leads to a hexagonal moiré superlattice. The long-range structure has a moiré unit cell (opaque overlay) with varying local stacking order AA/AB/BA, where A and B correspond to the two atomic sites in each of the stacked graphene unit cells. (b) Density of states (DOS) as a function of twist angle  $\alpha$ , showing peaks ascribed to emergent flat bands associated with three main pseudo-Landau levels (PLLs). Grey dotted lines denote the position of Fermi levels at half-filled  $\pm 1$ -PLL bands: The two 0-PLL bands near charge neutrality hold 4 electrons each; similarly, each of the  $\pm 1$ -PLL bands holds 4 electrons and thus is half-filled at a doping level of  $\pm 6$  electrons per moiré cell. At the flat-band angle  $\alpha^* = 0.8^\circ$ , the bandwidth of the  $\pm 1$ -PLLs becomes minimal. (c) Local density of states (LDOS) in the  $-1$ -PLL, showing the emergence of an effective triangular lattice of states localized around the AA regions. Dashed lines mark effective hopping amplitudes in an effective triangular superlattice Hamiltonian, see text. (d)–(f) Band structures for  $\alpha < \alpha^*$ ,  $\alpha = \alpha^*$  and  $\alpha > \alpha^*$  illustrating how the  $\pm 1$ -PLL bands evolve to generate flat bands at  $\alpha^*$  (marked in blue). (f) The 0-PLL flattens at the magic angle [15, 16]. Note that there is a gap to the  $\pm 1$ -PLLs (small in this plotted scale).

leading to electrically tunable magnetism. We thus arrive at a new platform where correlations and topology can be controlled at the same time.

Below, we start from the real-space bilayer tight-binding model and find flat bands at an angle  $\alpha^* = 0.8^\circ$ ; the states in these  $\pm 1$  PLLs are strongly localized on the triangular superlattice of the moiré structure. We include local interactions on a mean-field level and find the magnetic instability. In a third step, we include the interlayer bias

and map out the local Berry curvature in real-space that introduces band dispersion and consequently reduces the magnetic order.

Twisted bilayer graphene is formed by stacking two honeycomb lattices of carbon with a small twist angle  $\alpha$ , resulting in a moiré structure of (approximate) periodicity  $L_M$  that grows inversely with  $\alpha$ , see Fig. 1(a). This supercell can exceed the lattice constant  $a$  in size by 1–2 orders of magnitude and features regions with well-defined local stacking orders AA, AB and BA, with A and B denoting the inequivalent atomic sites in a each hexagonal unit cell. We model the twisted bilayer with a real-space tight-binding Hamiltonian

$$H_0 = \sum_{\langle i,j \rangle, s} t c_{i,s}^\dagger c_{j,s} + \sum_{i,j,s} t_{ij}^\pm c_{i,s}^\dagger c_{j,s} - \sum_{i,s} \mu c_{i,s}^\dagger c_{i,s}, \quad (1)$$

where  $c_{i,s}^{(\dagger)}$  destroys (creates) an electron at site  $\mathbf{r}_i = (x_i, y_i, z_i)$  in one of the layers ( $z_i = \pm d/2$ ) with spin  $s = \uparrow, \downarrow$  and  $\mu$  is the chemical potential;  $t$  is the nearest-neighbor hopping within each layer and  $t_{ij}^\pm = t_\perp [(z_i - z_j)^2 / |\mathbf{r}_i - \mathbf{r}_j|^2] e^{-(|\mathbf{r}_i - \mathbf{r}_j| - d)/\ell}$  is the twist-angle dependent hopping [40] from  $\mathbf{r}_i$  to  $\mathbf{r}_j$  with amplitude  $t_\perp \simeq 0.12t$ , range  $\ell \simeq 0.13a$ , and the interlayer distance  $d \simeq 1.4a$ . We utilize a scaling relation that brings the low-energy physics of small angles  $\alpha$  to larger ones by appropriately increasing the interlayer hopping amplitude  $t_\perp$  [31, 37, 41–43]. This allows us to perform our analysis at moiré unit cells that are small enough for numerical treatment.

The twist  $\alpha$  effectively creates a nonuniform interlayer hopping with a corresponding gauge field [29, 44]. This, in turn, leads to a destructive interference that generates our  $\pm 1$  PLL flat bands that naturally lend themselves for strong-correlation physics. In Fig. 1(b), we present the low-energy density of states (DOS) of the bilayer as a function of its twist angle. Three main PLL bands are indexed with  $-1, 0, 1$ , which become flat at the marked specific angles. In this work, we are interested in the  $\pm 1$  bands with states that are localized around the AA regions of the superlattice, see Fig. 1(c). At negative (positive) energies, as a function of the twist angle  $\alpha$ , the targeted band evolves from having a negative (positive) effective mass to a positive (negative) one, see Figs. 1(d)–(f). At our “flat-band” angle  $\alpha^* \simeq 0.8^\circ$  [Fig. 1(e)], we achieve maximal isolation of the  $\pm 1$  PLL bands in energy. They hold up to  $\pm 4$  electrons per moiré unit cell and doping with  $\pm 6$  electrons corresponds to their half-filling. Note that the two 0 PLL bands hold  $\pm 4$  electrons each and become flat and nearly-degenerate at the magic angle  $\alpha \simeq 1.1^\circ$  [14–16, 45–48].

The  $\pm 1$ -PLL states arrange in a triangular lattice of “flower”-shaped Wannier orbitals centered around the AA regions, see Fig. 1(c). The effective low-energy physics

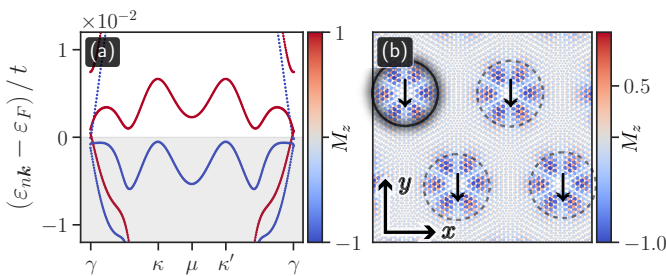


FIG. 2. Effect of local mean-field interactions [Eq. (2) with  $U = 2t$ ] in twisted bilayer graphene at physical twist angle  $\alpha^* = 0.8^\circ$ . (a) At  $-6$  electron doping, the half-filled flat band [cf. Fig. 1(e)] exhibits an exchange splitting between the up and down spins. (b) The resulting moiré structure of local magnetic moments. It forms a superlattice of finite collinear moments (circled “↓”) in real space. The red (blue) color indicates a positive (negative) local expectation value  $\langle S_z \rangle = M_z$  of the spin operator that is associated with a net ferromagnetic moment of each AA region and a weak local antiferromagnetic texture therein. For numerical calculation, we rescaled the parameters to  $\alpha \approx 2.86^\circ$ ,  $t_\perp = 0.46t$  [43].

for this triangular superlattice and its corresponding bands can be described by a single-site triangular-lattice tight-binding Hamiltonian with particles involving four flavors associated with spin and valley degrees of freedom and effective  $C_{3v}$ -symmetric hoppings. It is the absence of Dirac points in the minibands that enables such a triangular model that reproduces the band dispersion of the targeted band of the original bilayer tight-binding Hamiltonian [43]. In contrast, the nearly-flat bands at magic angles necessitate a description in terms of Wannier orbitals arranged on a *honeycomb* superlattice [45–49]. Our low-energy, four-flavor Hamiltonian is associated with an (approximate) local  $SU(4)$  symmetry; such a model has been predicted to display  $d + id$  superconductivity close to a Mott insulating state [50, 51], potentially providing a playground to realize unconventional interacting states.

We now explore the effect of electronic interactions at  $\alpha^*$  when the system is doped with  $\pm 6$  electrons. We introduce interactions in a minimal way using a local Hubbard term, yielding the interacting Hamiltonian  $H = H_0 + H_U$  with

$$H_U = U \sum_i n_{i\uparrow} n_{i\downarrow}, \quad (2)$$

where  $U$  is the interaction strength and  $n_{i,s} = c_{i,s}^\dagger c_{i,s}$  is the local density operator at each site. We chose the interaction strength  $U = 2t$  which accounts for a physical charging energy and our numerical rescaling, see Refs. [43, 52, 53]. We address this interaction term self-consistently using the spin-collinear mean-field ansatz  $n_{i\uparrow} n_{i\downarrow} \approx \langle n_{i\uparrow} \rangle \langle n_{i\downarrow} \rangle + n_{i\uparrow} \langle n_{i\downarrow} \rangle - \langle n_{i\uparrow} \rangle \langle n_{i\downarrow} \rangle$ . We find that the interaction [Eq. (2)] mainly affects the nearly-flat band of the superlattice, i.e., it induces a Stoner instability that splits the band, see Fig. 2(a). This interaction-induced ex-

change splitting is associated with a net magnetic moment of approximately  $2 \mu_B$  per moiré unit cell (obtained by integrating over the mildly-antiferromagnetic texture) aligned ferromagnetically between cells. Given the macrostructure of the system, this yields a triangular superlattice of local magnetic moments, see Fig. 2(b).

The emergence of magnetism in this flat-band angle regime is analogous to observations of magnetic instabilities at other angles and dopings [37, 38], in particular, in magic-angle superlattices [54–56]. Unique to our regime is the sensitivity of the  $\pm 1$ -PLL bands to an interlayer voltage-bias: as elaborated below, the latter modifies the electronic spectrum of the bilayer and hence allows for the tuning of the aforementioned magnetic order.

We now discuss the implications of an interlayer voltage-bias as described by the Hamiltonian  $H = H_0 + H_V$  (at  $U = 0$ ) with

$$H_V = \frac{V}{2} \sum_{i,s} \text{sgn}(z_i) c_{i,s}^\dagger c_{i,s}, \quad (3)$$

where  $V$  is the interlayer bias and  $\text{sgn}(z_i) = \pm 1$  for the top and bottom layers, respectively. This bias lowers the symmetry from  $C_{3v}$  to  $C_3$  by breaking the inversion symmetry between the layers. Finite  $V$  broadens and eventually washes out the singularity in the density of states [Fig. 3(a)] by introducing a dispersive valley-splitting into the band structure [Fig. 3(b)]. The substantial impact of the bias  $V$  on these flat bands is in stark contrast to the magic-angle regime, where it was found that a small bias has a negligible effect [21].

To better understand the mechanism that lifts the valley degeneracy, we analyze the spatial profile of the frequency-resolved valley Berry curvature [57]

$$\frac{\partial \Omega_v(\mathbf{r})}{\partial \omega} = \int_{\text{BZ}} \frac{d^2 k}{(2\pi)^2} \frac{\epsilon_{\alpha\beta}}{2} \langle \mathbf{r} | G_v(\partial_{k_\alpha} G_v^{-1})(\partial_{k_\beta} G_v) | \mathbf{r} \rangle, \quad (4)$$

where  $\int_{\text{BZ}} d^2 k \dots$  denotes integration over the Brillouin zone and  $\epsilon_{\alpha\beta}$  is the Levi-Civita tensor. We denote  $G_v = [\omega - H(\mathbf{k}) + i0^+]^{-1} \mathcal{P}_v$  as the Green’s function of the Bloch Hamiltonian  $H(\mathbf{k}) = H_0(\mathbf{k}) + H_V(\mathbf{k})$ , and  $\mathcal{P}_v$  is the valley polarization operator [31, 58, 59] that weighs the states with  $\pm 1$  depending on which graphene valley ( $K, K'$ ) they originate from. This allows us to find the valley-Chern number through integration over energies and over the unit cell, i.e.,  $C_v = \int_{\text{UC}} d^2 r \int_{-\infty}^{\mu} d\omega \partial_\omega \Omega_v(\mathbf{r})$ , which only takes nonzero values if time-reversal or inversion symmetry are broken. By breaking inversion symmetry, the interlayer bias  $V$  produces a finite valley-Chern number with the spatial texture in the Berry curvature as shown in Fig. 3(c), featuring alternating signs between AB/BA-stacked regions [13, 60, 61]. These, in turn, can be interpreted as a fake staggered valley magnetic field. At smaller

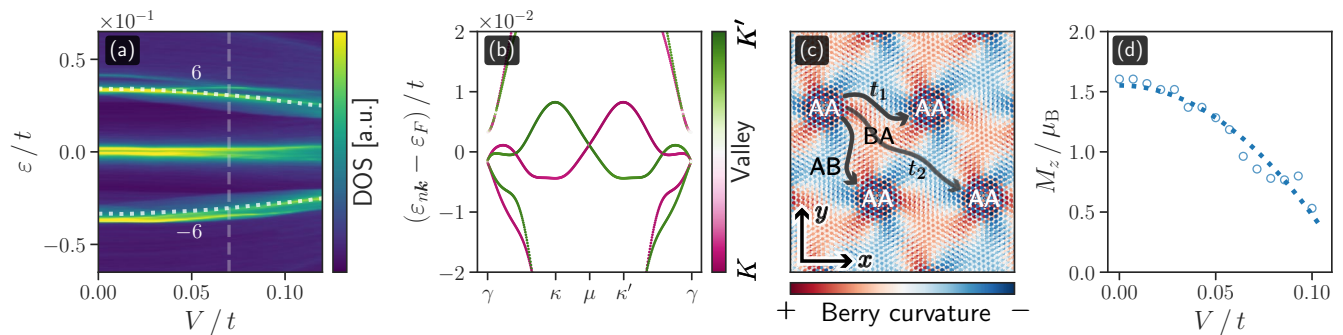


FIG. 3. Effects of interlayer bias  $V$  on the flat bands of bilayer graphene at twist angle  $\alpha^* = 0.8^\circ$ , (a)–(c) without and (d) with interactions. (a) The sharp peaks in the density of states (DOS) broaden and vanish with increasing interlayer bias  $V$ ; *dotted lines* mark Fermi energies for dopings  $\pm 6$ . (b) At  $-6$  electron doping, the half-filled flat bands disperse upon introduction of a small interlayer voltage bias [ $V/t = 0.07$ , *dashed line* in panel (a)] to form two independent valley-polarized bands (*green and purple*) [cf. Fig. 1(e)]. (c) The local valley Berry curvature in position space  $\partial\Omega_v(\mathbf{r})/\partial\omega$  [Eq. (4)] (integrated over the bands shown in b) can be understood in terms of an emergent valley magnetic field in the AB/BA regions. This field destroys the fine-tuned interference, inducing a finite bandwidth in the originally flat bands. (d) The total interaction-induced [ $U = 2t$ ] mean-field magnetization  $M_z$  at the twist angle  $\alpha^*$  decreases with interlayer bias  $V$ . The bias-induced dispersion quenches the interactions and the formation of magnetic order. For numerical calculation, we rescaled the physical parameters to  $\alpha \approx 2.86^\circ$ ,  $t_\perp = 0.46t$  [43].

angles  $\alpha < \alpha^*$ , this spatial texture in the Berry curvature sharpens up and eventually leads to the valley helical networks [36] recently observed in experiments [11].

If we regard the formation of flat bands in Fig. 1(e) as the result of fine-tuned destructive interference between neighboring Wannier orbitals [15, 16], we can explain how the dispersive valley-splitting in Fig. 3(b) arises: the emergent valley-chiral magnetic field induced by the interlayer bias *alters* the relative phases between the Wannier orbitals, and creates additional valley-splittings. This effect can be captured by the effective triangular superlattice Hamiltonian via the inclusion of Peierls phases in the hoppings [43]. These phases correspond to a finite magnetic flux per triangle that averages to zero over one unit cell, see Fig. 3(c), reminiscent of Haldane’s model for Chern insulators [62]. As the two valleys are time-reversal-symmetric partners these fluxes have opposite sign, thus canceling one another locally. To summarize, the interlayer bias in the full model takes the role of the valley-magnetic flux per plaquette in the low-energy model.

We can now analyze how the interlayer bias affects the interaction-induced correlated state by considering the Hamiltonian  $H = H_0 + H_U + H_V$ . We expect that the interlayer-bias-induced band dispersion modifies the magnetic state discussed in Fig. 2. Indeed, as shown in Fig. 3(d), the ground state magnetization is substantially quenched even for moderate bias ( $V \approx 100$  meV). Hence, the interlayer bias serves as an external control for the correlated state at our *flat-band-angle*. We once more emphasize that this feature is in striking contrast to magic-angle graphene, where a small interlayer bias does not substantially change the correlated state [21].

There are three interesting avenues for further investi-

gations beyond the scope of this work. First, we emphasize that our analysis does not take into account possible lattice relaxations [63, 64], which may impact the specific angle at which the targeted band becomes sufficiently flat. Second, the existence of twist-angle disorder [65] is likely to modify the width of the targeted band and uniform twist angles may be required in order to observe the correlated state – similarly to the phenomenology shown at the magic angle [22]. Third, the triangular nature of the superlattice suggests that a spin-spiral state may exist that is energetically competitive with the ferromagnetic configuration discussed above. Indeed, we performed our self-consistent mean-field analysis for several candidates and found indications for a  $120^\circ$  spin-spiral state (maximally antiferromagnetic) that competes with the collinear order. This observation leads us to conclude that the system is profoundly frustrated, with sizable antiferromagnetic exchange coupling to second-neighbor moiré cells. Since such triangular lattices have been proposed to give rise to spin-liquid phases [66], further investigations into our proposed flat-band system might unveil a nontrivial realization of such physics.

To summarize, we have shown that electronic correlations can arise in twisted graphene bilayers at fillings of 6 electrons/holes per moiré unit cell. This correlated regime is shown to appear at angles around  $0.8^\circ$  at doping levels of  $\pm 6$  electrons per moiré unit cell, for which the chemical potential falls into one of the  $\pm 1$ -pseudo-Landau levels. For that regime, we show that interactions promote the formation of local magnetic moments in the moiré supercells arranging on a triangular lattice. Furthermore, we have shown that the interlayer bias can be used to control the magnetic instability. The origin of this tunability was

demonstrated to be related to the control over an effective staggered valley-magnetic field in the heterostructure, that modifies fine-tuned interferences in the superlattice states, thereby substantially affecting the low-energy dispersion. Our results put forward a new regime in twisted graphene multilayers hosting correlations that result in a magnetic instability that is highly tunable with weak interlayer biases.

We acknowledge financial support from the Swiss National Science Foundation. J. L. L. acknowledges financial support from the ETH Fellowship program.

- 
- [1] I. Bloch, J. Dalibard, and W. Zwerger, Many-body physics with ultracold gases, *Rev. Mod. Phys.* **80**, 885 (2008).
- [2] A. Mazurenko, C. S. Chiu, G. Ji, M. F. Parsons, M. Kanász-Nagy, R. Schmidt, F. Grusdt, E. Demler, D. Greif, and M. Greiner, A cold-atom fermi-hubbard antiferromagnet, *Nature* **545**, 462 (2017).
- [3] T. Uehlinger, G. Jotzu, M. Messer, D. Greif, W. Hofstetter, U. Bissbort, and T. Esslinger, Artificial graphene with tunable interactions, *Phys. Rev. Lett.* **111**, 185307 (2013).
- [4] R. Toskovic, R. van den Berg, A. Spinelli, I. S. Eliens, B. van den Toorn, B. Bryant, J.-S. Caux, and A. F. Otte, Atomic spin-chain realization of a model for quantum criticality, *Nature Physics* **12**, 656 (2016).
- [5] S. Loth, S. Baumann, C. P. Lutz, D. M. Eigler, and A. J. Heinrich, Bistability in atomic-scale antiferromagnets, *Science* **335**, 196 (2012).
- [6] A. H. Castro Neto, F. Guinea, N. M. R. Peres, K. S. Novoselov, and A. K. Geim, The electronic properties of graphene, *Rev. Mod. Phys.* **81**, 109 (2009).
- [7] A. K. Geim and I. V. Grigorieva, Van der waals heterostructures, *Nature* **499**, 419 (2013).
- [8] T. M. R. Wolf, O. Zilberberg, I. Levkivskiy, and G. Blatter, Substrate-induced topological minibands in graphene, *Phys. Rev. B* **98**, 125408 (2018).
- [9] Y. Cao, V. Fatemi, A. Demir, S. Fang, S. L. Tomarken, J. Y. Luo, J. D. Sanchez-Yamagishi, K. Watanabe, T. Taniguchi, E. Kaxiras, R. C. Ashoori, and P. Jarillo-Herrero, Correlated insulator behaviour at half-filling in magic-angle graphene superlattices, *Nature* **556**, 80 (2018).
- [10] Y. Cao, V. Fatemi, S. Fang, K. Watanabe, T. Taniguchi, E. Kaxiras, and P. Jarillo-Herrero, Unconventional superconductivity in magic-angle graphene superlattices, *Nature* **556**, 43 (2018).
- [11] P. Rickhaus, J. Wallbank, S. Slizovskiy, R. Pisoni, H. Overweg, Y. Lee, M. Eich, M.-H. Liu, K. Watanabe, T. Taniguchi, T. Ihn, and K. Ensslin, Transport through a network of topological channels in twisted bilayer graphene, *Nano Letters* **18**, 6725 (2018).
- [12] R. Ribeiro-Palau, C. Zhang, K. Watanabe, T. Taniguchi, J. Hone, and C. R. Dean, Twistable electronics with dynamically rotatable heterostructures, *Science* **361**, 690 (2018).
- [13] E. V. Castro, K. S. Novoselov, S. V. Morozov, N. M. R. Peres, J. M. B. L. dos Santos, J. Nilsson, F. Guinea, A. K. Geim, and A. H. C. Neto, Biased bilayer graphene: Semiconductor with a gap tunable by the electric field effect, *Phys. Rev. Lett.* **99**, 216802 (2007).
- [14] J. M. B. Lopes dos Santos, N. M. R. Peres, and A. H. Castro Neto, Graphene bilayer with a twist: Electronic structure, *Phys. Rev. Lett.* **99**, 256802 (2007).
- [15] E. Suárez Morell, J. D. Correa, P. Vargas, M. Pacheco, and Z. Barticevic, Flat bands in slightly twisted bilayer graphene: Tight-binding calculations, *Phys. Rev. B* **82**, 121407 (2010).
- [16] R. Bistritzer and A. H. MacDonald, Moire bands in twisted double-layer graphene, *Proceedings of the National Academy of Sciences* **108**, 12233 (2011).
- [17] N. Bultinck, S. Chatterjee, and M. P. Zaletel, Anomalous Hall ferromagnetism in twisted bilayer graphene, arXiv e-prints , arXiv:1901.08110 (2019), arXiv:1901.08110 [cond-mat.str-el].
- [18] Y.-H. Zhang, D. Mao, and T. Senthil, Twisted Bilayer Graphene Aligned with Hexagonal Boron Nitride: Anomalous Hall Effect and a Lattice Model, (2019), arXiv:1901.08209.
- [19] Y. Cao, D. Chowdhury, D. Rodan-Legrain, O. Rubies-Bigordà, K. Watanabe, T. Taniguchi, T. Senthil, and P. Jarillo-Herrero, Strange metal in magic-angle graphene with near Planckian dissipation, arXiv e-prints , arXiv:1901.03710 (2019), arXiv:1901.03710 [cond-mat.str-el].
- [20] Y. Jiang, J. Mao, X. Lai, K. Watanabe, T. Taniguchi, K. Haule, and E. Y. Andrei, Evidence of charge-ordering and broken rotational symmetry in magic angle twisted bilayer graphene, arXiv e-prints , arXiv:1904.10153 (2019), arXiv:1904.10153 [cond-mat.mes-hall].
- [21] M. Yankowitz, S. Chen, H. Polshyn, Y. Zhang, K. Watanabe, T. Taniguchi, D. Graf, A. F. Young, and C. R. Dean, Tuning superconductivity in twisted bilayer graphene, *Science* **363**, 1059 (2019).
- [22] X. Lu, P. Stepanov, W. Yang, M. Xie, M. A. Aamir, I. Das, C. Urgell, K. Watanabe, T. Taniguchi, G. Zhang, A. Bachtold, A. H. MacDonald, and D. K. Efetov, Superconductors, Orbital Magnets, and Correlated States in Magic Angle Bilayer Graphene, arXiv e-prints , arXiv:1903.06513 (2019), arXiv:1903.06513 [cond-mat.str-el].
- [23] J. Liu, J. Liu, and X. Dai, Pseudo landau level representation of twisted bilayer graphene: Band topology and implications on the correlated insulating phase, *Phys. Rev. B* **99**, 155415 (2019).
- [24] G. Tarnopolsky, A. J. Kruchkov, and A. Vishwanath, Origin of magic angles in twisted bilayer graphene, *Phys. Rev. Lett.* **122**, 106405 (2019).
- [25] H. Shi, Z. Zhan, Z. Qi, K. Huang, E. van Veen, J. A. Silva-Guillén, R. Zhang, P. Li, K. Xie, H. Ji, M. I. Katsnelson, S. Yuan, S. Qin, and Z. Zhang, Large-area, periodic, and tunable pseudomagnetic fields in low-angle twisted bilayer graphene, arXiv e-prints , arXiv:1905.04515 (2019), arXiv:1905.04515 [cond-mat.str-el].
- [26] M. Vozmediano, M. Katsnelson, and F. Guinea, Gauge fields in graphene, *Physics Reports* **496**, 109 (2010).
- [27] T. Low and F. Guinea, Strain-induced pseudomagnetic field for novel graphene electronics, *Nano Letters* **10**, 3551 (2010).
- [28] Y. Jiang, J. Mao, J. Duan, X. Lai, K. Watanabe, T. Taniguchi, and E. Y. Andrei, Visualizing strain-induced pseudomagnetic fields in graphene through an hBN magnifying glass, *Nano Letters* **17**, 2839 (2017).
- [29] P. San-Jose, J. González, and F. Guinea, Non-abelian gauge potentials in graphene bilayers, *Phys. Rev. Lett.* **108**, 216802 (2012).
- [30] J. Liu and X. Dai, Quantum valley hall effect, orbital magnetism, and anomalous hall effect in twisted multilayer graphene systems, arXiv e-prints , arXiv:1903.10419 (2019), arXiv:1903.10419.
- [31] A. Ramires and J. L. Lado, Electrically tunable gauge fields in tiny-angle twisted bilayer graphene, *Phys. Rev. Lett.* **121**, 146801 (2018).

- [32] Z. Ma, S. Li, Y.-W. Zheng, M.-M. Xiao, H. Jiang, J.-H. Gao, and X. C. Xie, Topological flat bands in twisted trilayer graphene, arXiv e-prints , arXiv:1905.00622 (2019), arXiv:1905.00622 [cond-mat.mes-hall].
- [33] N. Raju Chebrolu, B. Lingam Chittari, and J. Jung, Flatbands in twisted bi-bilayer graphene, arXiv e-prints , arXiv:1901.08420 (2019), arXiv:1901.08420 [cond-mat.mes-hall].
- [34] Y. H. Zhang, D. Mao, Y. Cao, P. Jarillo-Herrero, and T. Senthil, Nearly flat Chern bands in moiré superlattices, *Phys. Rev. B* **99**, 1 (2019).
- [35] M. H. Naik and M. Jain, Ultraflatbands and shear solitons in moiré patterns of twisted bilayer transition metal dichalcogenides, *Phys. Rev. Lett.* **121**, 266401 (2018).
- [36] P. San-Jose and E. Prada, Helical networks in twisted bilayer graphene under interlayer bias, *Phys. Rev. B* **88**, 121408 (2013).
- [37] L. A. Gonzalez-Arraga, J. L. Lado, F. Guinea, and P. San-Jose, Electrically controllable magnetism in twisted bilayer graphene, *Phys. Rev. Lett.* **119**, 107201 (2017).
- [38] A. O. Sboychakov, A. V. Rozhkov, A. L. Rakhmanov, and F. Nori, Externally controlled magnetism and band gap in twisted bilayer graphene, *Phys. Rev. Lett.* **120**, 266402 (2018).
- [39] A. Lopez-Bezanilla, Emergence of flat-band magnetism and half-metallicity in twisted bilayer graphene, *Phys. Rev. Materials* **3**, 054003 (2019).
- [40] A. O. Sboychakov, A. L. Rakhmanov, A. V. Rozhkov, and F. Nori, Electronic spectrum of twisted bilayer graphene, *Phys. Rev. B* **92**, 075402 (2015).
- [41] M.-H. Liu, P. Rickhaus, P. Makk, E. Tóvári, R. Maurand, F. Tkatschenko, M. Weiss, C. Schönenberger, and K. Richter, Scalable tight-binding model for graphene, *Phys. Rev. Lett.* **114**, 036601 (2015).
- [42] S. Carr, S. Fang, P. Jarillo-Herrero, and E. Kaxiras, Pressure dependence of the magic twist angle in graphene superlattices, *Phys. Rev. B* **98**, 085144 (2018).
- [43] See supplemental material for more details on (I) the numerical parameters, on (II) the low-energy model and on (III) the nature of the charging energy.
- [44] L.-J. Yin, J.-B. Qiao, W.-J. Zuo, W.-T. Li, and L. He, Experimental evidence for non-abelian gauge potentials in twisted graphene bilayers, *Phys. Rev. B* **92**, 081406 (2015).
- [45] M. Koshino, N. F. Q. Yuan, T. Koretsune, M. Ochi, K. Kuroki, and L. Fu, Maximally localized wannier orbitals and the extended hubbard model for twisted bilayer graphene, *Phys. Rev. X* **8**, 031087 (2018).
- [46] H. C. Po, L. Zou, A. Vishwanath, and T. Senthil, Origin of mott insulating behavior and superconductivity in twisted bilayer graphene, *Phys. Rev. X* **8**, 031089 (2018).
- [47] J. Kang and O. Vafek, Symmetry, maximally localized wannier states, and a low-energy model for twisted bilayer graphene narrow bands, *Phys. Rev. X* **8**, 031088 (2018).
- [48] J. Ahn, S. Park, and B.-J. Yang, Failure of Nielsen-Ninomiya theorem and fragile topology in two-dimensional systems with space-time inversion symmetry: application to twisted bilayer graphene at magic angle, arXiv e-prints , arXiv:1808.05375 (2018), arXiv:1808.05375 [cond-mat.mes-hall].
- [49] B. Roy and V. Juričić, Unconventional superconductivity in nearly flat bands in twisted bilayer graphene, *Phys. Rev. B* **99**, 1 (2019).
- [50] C. Xu and L. Balents, Topological superconductivity in twisted multilayer graphene, *Phys. Rev. Lett.* **121**, 087001 (2018).
- [51] X.-C. Wu, A. Keselman, C.-M. Jian, K. A. Pawlak, and C. Xu, Ferromagnetism and Spin-Valley liquid states in Moiré {e} Correlated Insulators, arXiv e-prints , arXiv:1905.00033 (2019), arXiv:1905.00033 [cond-mat.str-el].
- [52] F. Guinea and N. R. Walet, Electrostatic effects, band distortions, and superconductivity in twisted graphene bilayers, *Proceedings of the National Academy of Sciences* **115**, 13174 (2018), <https://www.pnas.org/content/115/52/13174.full.pdf>.
- [53] T. Cea, N. R. Walet, and F. Guinea, Electronic bandwidth and pinning of Fermi energy to van Hove singularities in twisted bilayer graphene: a self consistent approach, arXiv e-prints , arXiv:1906.10570 (2019), arXiv:1906.10570 [cond-mat.str-el].
- [54] A. Thomson, S. Chatterjee, S. Sachdev, and M. S. Scheurer, Triangular antiferromagnetism on the honeycomb lattice of twisted bilayer graphene, *Phys. Rev. B* **98**, 075109 (2018).
- [55] K. Seo, V. N. Kotov, and B. Uchoa, Ferromagnetic Mott State in Twisted Graphene Bilayers at the Magic Angle, arXiv e-prints , arXiv:1812.02550 (2018), arXiv:1812.02550 [cond-mat.str-el].
- [56] J. Kang and O. Vafek, Strong coupling phases of partially filled twisted bilayer graphene narrow bands, arXiv e-prints , arXiv:1810.08642 (2018), arXiv:1810.08642 [cond-mat.str-el].
- [57] K.-T. Chen and P. A. Lee, Unified formalism for calculating polarization, magnetization, and more in a periodic insulator, *Phys. Rev. B* **84**, 205137 (2011).
- [58] E. Colomé and M. Franz, Antichiral edge states in a modified haldane nanoribbon, *Phys. Rev. Lett.* **120**, 086603 (2018).
- [59] A. Ramires and J. L. Lado, Impurity-induced triple point fermions in twisted bilayer graphene, arXiv e-prints , arXiv:1902.05862 (2019), arXiv:1902.05862 [cond-mat.mes-hall].
- [60] F. Zhang, A. H. MacDonald, and E. J. Mele, Valley chern numbers and boundary modes in gapped bilayer graphene, *Proceedings of the National Academy of Sciences* **110**, 10546 (2013).
- [61] Q. Tong, H. Yu, Q. Zhu, Y. Wang, X. Xu, and W. Yao, Topological mosaics in moiré superlattices of van der waals hetero-bilayers, *Nature Physics* **13**, 356 (2016).
- [62] F. D. M. Haldane, Model for a quantum hall effect without landau levels: Condensed-matter realization of the "parity anomaly", *Phys. Rev. Lett.* **61**, 2015 (1988).
- [63] N. N. T. Nam and M. Koshino, Lattice relaxation and energy band modulation in twisted bilayer graphene, *Phys. Rev. B* **96**, 075311 (2017).
- [64] P. Lucignano, D. Alfè, V. Cataudella, D. Ninno, and G. Cantele, Crucial role of atomic corrugation on the flat bands and energy gaps of twisted bilayer graphene at the magic angle  $\theta \sim 1.08^\circ$ , *Phys. Rev. B* **99**, 195419 (2019).
- [65] T. E. Beechem, T. Ohta, B. Diaconescu, and J. T. Robinson, Rotational disorder in twisted bilayer graphene, *ACS Nano* **8**, 1655 (2014).
- [66] R. Kaneko, S. Morita, and M. Imada, Gapless spin-liquid phase in an extended spin 1/2 triangular heisenberg model, *Journal of the Physical Society of Japan* **83**, 093707 (2014).

## Supplementary material for “Electrically Tunable Flat Bands and Magnetism in Twisted Bilayer Graphene”

T. M. R. Wolf, J. L. Lado, G. Blatter, and O. Zilberberg

*Institute for Theoretical Physics, ETH Zurich, 8093 Zurich, Switzerland*

(Dated: September 4, 2019)

In this supplemental material, we provide additional details on (i) methods used for the analysis of the microscopic model of the twisted bilayer (section I) and (ii) the effective (phenomenological) low-energy model describing the triangular lattice of localized AA Wannier orbital, as well as its effectiveness in capturing the effects observed in the main text (section II). Specifically, using (ii), we discuss how the emergence of flat bands  $\pm 1$ -PLLs can be understood to be a result of destructive interference (i.e., suppressed hopping amplitudes) and how the interlayer bias (interpreted as Haldane-like valley-flux texture in the moiré supercell) detunes the interference and induces valley-dependent dispersion.

### I. METHODS FOR ANALYZING THE MICROSCOPIC TIGHT-BINDING MODEL

In the main text, we model the non-interacting twisted bilayer with a real-space tight-binding Hamiltonian [see Eqs. (1) and (3) in the main text]. The spectrum of the twisted bilayer system results from backfolding and hybridizing the graphene bands of both layers in a mini-Brillouin zone. In the current work, the spectrum is obtained using exact diagonalization. Due to computational resource bounds, this exact approach limits how large we can choose our moiré unit cells. To reduce the size of the unit cells (and hence the number of atoms within them), we use the property that the low-energy bands at small angles only depend on the ratio  $t_{\perp}/\sin(\alpha/2)$  [1–4], i.e., we can bring the low-energy physics of smaller angles to larger ones by increasing the interlayer coupling  $t_{\perp}$ , or more precisely:  $\alpha \rightarrow \alpha'$  with  $t_{\perp} \rightarrow t_{\perp} \sin(\alpha'/2)/\sin(\alpha/2)$  and  $t \rightarrow t \sin(\alpha'/2)$ .

To produce Fig. 1, we use the parameters  $t_{\perp} = 0.23t$ ,  $V = 0$  and twist angles  $\alpha_{n,1} \approx 5.1^{\circ}, \dots, 1.12^{\circ}$  with  $n = 6, \dots, 29$ . Making use of the scaling transformation, this corresponds to the physically realistic parameters  $t'_{\perp} = 0.12t$  with  $\alpha'$  between  $0.57^{\circ}$  and  $1.12^{\circ}$ . To produce Fig. 2, we use  $t_{\perp} = 0.46t$ ,  $V = 0$  and  $\alpha_{11,1} \approx 2.86^{\circ}$ , which is the rescaled equivalent of  $t'_{\perp} = 0.12t$  for twist angle  $\alpha' = 0.8^{\circ}$ . To produce Fig. 3, we use the same parameters as in Fig. 2, but in (a),(d) we vary  $V = 0, \dots, 0.12t$ , in (b),(c)  $V = 0.07t$ .

### II. EFFECTIVE TRIANGULAR TIGHT-BINDING MODEL DESCRIBING THE $\pm 1$ -PLLs

The texture of the local density of states for the  $\pm 1$  PLL bands [cf. Fig. 1(c)] suggests that the eigenstates within these bands form Wannier-orbitals around the AA regions that are coupled on a triangular lattice. Furthermore, these Wannier orbitals are spin-degenerate and independently result from both valley degrees of freedom of the bilayer, see Fig. S1(a). We can, therefore, coarse grain these orbitals to effective atomic sites and describe their coupling using a tight-binding model

$$H_{\text{eff}} = \sum_{\langle \eta \eta' \rangle, \sigma} \gamma_1 d_{\eta \sigma}^{\dagger} d_{\eta' \sigma} + \sum_{\langle\langle \eta \eta' \rangle\rangle, \sigma} \gamma_2 d_{\eta \sigma}^{\dagger} d_{\eta' \sigma}, \quad (\text{S1})$$

where  $\sigma = (s, \nu)$  labels the four orbitals (spin  $s = \uparrow, \downarrow$  and valley  $\nu = \pm$ ), and  $d_{\eta \sigma}^{\dagger}$  destroys (creates) an electron in the respective Wannier orbital in AA region  $\eta$ .  $\gamma_1$  and  $\gamma_2$  are real nearest and next-nearest hopping amplitudes respecting  $C_{3v}$  symmetry.

### A. Flat band through destructive interference

Generally, the effective hopping in the low-energy model (S1) is controlled by the twist angle  $\alpha$  and the interlayer hopping  $t_{\perp}$  in the microscopic model, i.e.,  $\gamma_i \equiv \gamma_i(\alpha, t_{\perp})$ . In Fig. S2, we fit the effective hopping amplitudes  $\gamma_1$  and  $\gamma_2$  such that we can phenomenologically reproduce the  $-1$ -PLL band dispersion in Figs. 1(d)–(f).

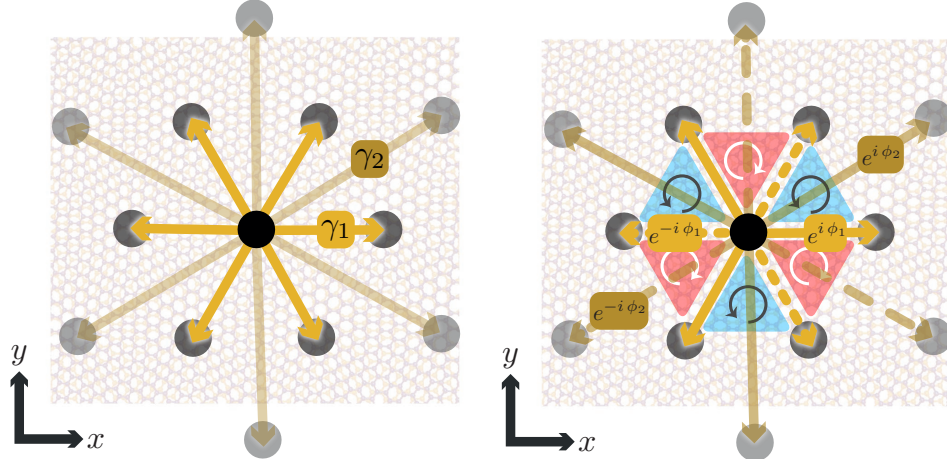


FIG. S1. Sketch of the effective superlattice for Wannier states localized near AA stacked regions (black circles) in the moiré structure (a) without interlayer bias and (b) and with finite interlayer bias  $V > 0$ . The effective physics of the  $\pm 1$  PLL bands is captured by nearest- and next-nearest-neighbor hopping amplitudes  $\gamma_1$  and  $\gamma_2$ . The interlayer bias induces complex phases in  $\gamma_1$  and  $\gamma_2$  that encode the emergent valley magnetic flux texture piercing the triangular unit cells (red/ $\cup$ , and blue/ $\cup$  in- and out-of-plane flux, respectively).

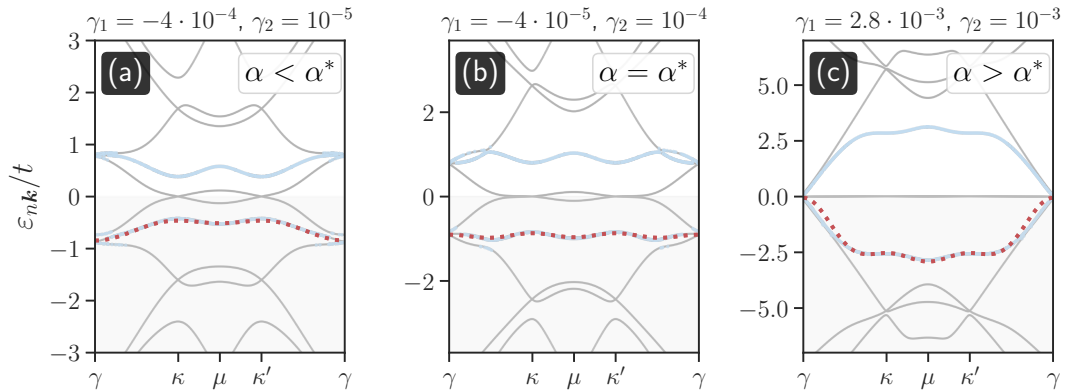


FIG. S2. Band dispersion of the effective model (S1) (dotted red) such that it fits the  $-1$ -PLL band dispersion of the twisted bilayer graphene (pale blue) for different twist angles (a)  $\alpha < \alpha^*$ , (b)  $\alpha = \alpha^*$ , and (c)  $\alpha > \alpha^*$  [cf. Figs. 1(d)–(f)]. We see that the effective hopping parameter  $\gamma_1$  of the dispersive band in (a) and (c) switches sign while  $\gamma_2$  remains approximately constant. This, in turn, generates the negative and positive effective mass of the band. At the transition (b),  $\gamma_1 \sim 0$  and the band flattens.



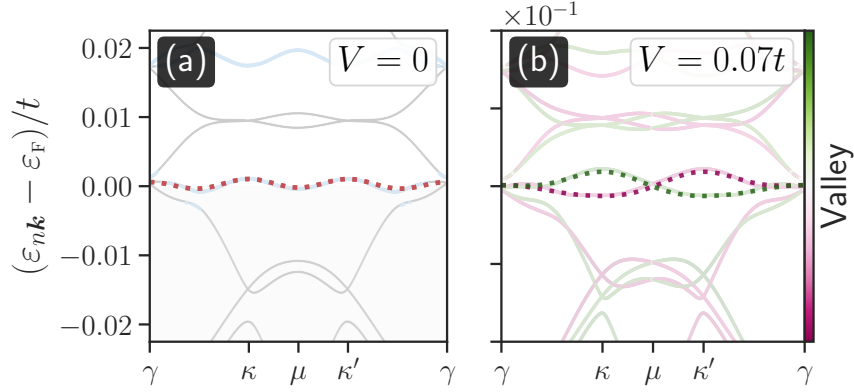


FIG. S3. Band dispersion of the effective triangular model (S1) once complex hopping amplitudes (S2) have been incorporated in order to account for the valley-flux. The effective band dispersion was fitted to that of the  $-1$ -PLL band of twisted bilayer graphene (*pale colors*) for different voltage-bias (a)  $V = 0$  and (b)  $V = 0.07t$  [cf. Fig. 3(b)]. As discussed in the main text, the emergent valley-magnetic fluxes (that are induced by the interlayer bias) lift the (approximate) valley degeneracy.

### B. Interlayer voltage bias as valley-flux

As discussed in the main text, a voltage-bias between the twisted graphene layers breaks inversion symmetry and consequently lifts the degeneracy between the two valleys of the material. Our analysis of the valley Berry curvature revealed a fake valley (or ‘chiral’) magnetic field that we can incorporate into our single-site four-orbital triangular hopping model (S1) via a Peierl’s substitution with opposing fluxes between the two valleys, i.e.,

$$\gamma_j \mapsto \gamma_j e^{i\nu 2\pi \phi_j}, \quad (\text{S2})$$

where  $\nu = \pm$  is again the valley degree of freedom. The phases should be compatible with the Haldane-like valley flux pattern in Fig. 3(c), i.e.,  $0 < \phi_1 < 1$  and  $0 \leq \phi_2 \ll 1$ .

In Fig. S3, we show that by selecting the appropriate hopping parameters  $\gamma_j$  and phases  $\phi_j$  reproduces the interlayer bias-induced valley splitting. The parameters of panel (a) are the same as in Fig. S2(b) and those for panel (b) have phases  $\phi_1 = 0.75$  and  $\phi_2 = 0.1$ .

## III. ELECTRONIC INTERACTIONS IN TWISTED MULTILAYER GRAPHENE

### A. Hubbard versus screened Coulomb interactions

In twisted graphene multilayers, the long-ranged part of the Coulomb interaction is known to enhance the correlated gaps that emerge in flat-band regimes [5, 6]. In what follows, we show this enhancement by comparing the band dispersion of the (self-consistent) mean-field Hamiltonians for (a) a local Hubbard interaction with (b) that of (screened) Coulomb interaction. To that end, let us consider the more generic interaction

$$H_U = \sum_{i,j} V(|\mathbf{r}_i - \mathbf{r}_j|) n_{i\uparrow} n_{j\downarrow}, \quad (\text{S3})$$

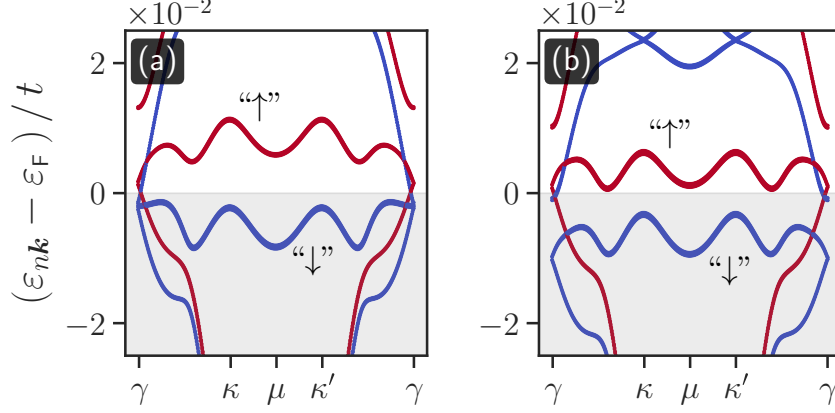


FIG. S4. Band dispersion in presence of electronic interactions [see Eq. (S3)] for (a) onsite Hubbard repulsion  $U_0 = 2t$  ( $V_0 = 0$ ) and for (b) reduced Hubbard repulsion  $U_0 = 0.5t$  but in presence of screened Coulomb interactions ( $V_0 = 0.37t$  and  $\lambda^{-1} = a$ , where  $a$  is the inter-atom distance); obtained from self-consistent mean-field iteration. Near the chemical potential, the two band dispersions are qualitatively very similar, showing that the long-ranged part of the interaction effectively renormalizes the onsite Hubbard repulsion. Note that we used a twist angle  $\alpha_{n,1}$  with  $n = 8$ .

where  $n_{i,s} = c_{i,s}^\dagger c_{i,s}$  is the local density operator at each positions  $\mathbf{r}_i$  and  $V(r)$  is the two-particle interaction. The latter shall contain two contributions: an onsite (Hubbard) repulsion  $U_0$  and a long-ranged Coulomb potential with screening length  $\lambda^{-1}$ , i.e.,

$$V(r) = \begin{cases} U_0, & \text{for } r = 0 \\ \frac{V_0}{r} e^{-\lambda(r-a)} & \text{for } r \neq 0, \end{cases} \quad (\text{S4})$$

where  $a$  the carbon-carbon distance. Note that  $V_0 = 0$  recovers the Hubbard Hamiltonian used in the main text.

As in the main text, we perform a mean-field decoupling in Eq. (S3), i.e.,  $n_{i\uparrow}n_{i\downarrow} \approx \langle n_{i\uparrow} \rangle n_{i\downarrow} + n_{i\uparrow} \langle n_{i\downarrow} \rangle - \langle n_{i\uparrow} \rangle \langle n_{i\downarrow} \rangle$ . We again iterate self-consistently to obtain the ground state of the mean-field Hamiltonian  $H_0 + H_V$ . Fig. S4 shows the self-consistent bandstructure for (a) the pure Hubbard case ( $V_0 = 0$ ,  $U_0 = 2t$ ) that we considered in the main text, and (b) the screened Coulomb case with a reduced onsite repulsion  $U_0 = 0.5t$  and  $V_0 = 0.37t$ . Both systems show a similar exchange splitting, despite a significantly smaller local interaction  $U_0$  in case (b). We conclude that the effect of a (more realistic) screened Coulomb interaction on the minibands near the chemical potential can be qualitatively reproduced by renormalizing (enhancing) the onsite repulsion and discarding the long-ranged term in the Hamiltonian.

### B. Rescaling the interaction strength along with the unit cell

As explained above (see section I), we rescaled our unit cells and interlayer hopping amplitudes towards larger angles, i.e.  $\alpha \rightarrow \alpha' = \lambda \alpha$  with  $t_\perp \rightarrow t'_\perp = \lambda t_\perp$ . In what follows, we deduce the scaling of the interaction strength  $U_0$  from the charging energy  $U_{\text{eff}} = U_0/N$  of the low-energy states [5]. Here,  $N$  is the number of atoms per moiré cell and grows inversely with  $\alpha^2$  (it is proportional to the area of the unit cell). To keep the low-energy physics unchanged, we have to keep the ratio of typical bandwidths and charging energy fixed when performing the rescaling:

$$U_0/t_\perp = U'_0/t'_\perp \quad \text{for} \quad \alpha \rightarrow \alpha' = \lambda \alpha, \quad t_\perp \rightarrow t'_\perp = \lambda t_\perp, \quad N \rightarrow N' = \lambda^{-2} N. \quad (\text{S5})$$

This yields the rescaled Hubbard interaction  $U'_0 = \lambda^{-1} U_0$ .

For the parameters of our system, this would imply using a value  $U_0 \approx 0.6t$  for  $n = 11$  for the realistic interaction term of Eq. (S3), together with the long-range part of the Coulomb interaction. We note that performing non-local mean-field calculations is substantially more computationally demanding than local ones. For this reason, in the main manuscript we have captured the effect of the non-local term by a renormalized local Hubbard Hamiltonian, namely taking  $U_0 = 2t$  and  $V = 0$  in Eq. (S3), as shown in Fig. S4(a) (see section III A). This choice of parameters yields a physical charging energy of 30 meV at  $\alpha \approx 0.8^\circ$ , similar to charging energies at the magic angle.

- 
- [1] M.-H. Liu, P. Rickhaus, P. Makk, E. Tóvári, R. Maurand, F. Tkatschenko, M. Weiss, C. Schönenberger, and K. Richter, Scalable tight-binding model for graphene, *Phys. Rev. Lett.* **114**, 036601 (2015).
  - [2] L. A. Gonzalez-Arraga, J. L. Lado, F. Guinea, and P. San-Jose, Electrically controllable magnetism in twisted bilayer graphene, *Phys. Rev. Lett.* **119**, 107201 (2017).
  - [3] A. Ramires and J. L. Lado, Electrically tunable gauge fields in tiny-angle twisted bilayer graphene, *Phys. Rev. Lett.* **121**, 146801 (2018).
  - [4] S. Carr, S. Fang, P. Jarillo-Herrero, and E. Kaxiras, Pressure dependence of the magic twist angle in graphene superlattices, *Phys. Rev. B* **98**, 085144 (2018).
  - [5] F. Guinea and N. R. Walet, Electrostatic effects, band distortions, and superconductivity in twisted graphene bilayers, *Proceedings of the National Academy of Sciences* **115**, 13174 (2018), <https://www.pnas.org/content/115/52/13174.full.pdf>.
  - [6] T. Cea, N. R. Walet, and F. Guinea, Electronic bandwidth and pinning of Fermi energy to van Hove singularities in twisted bilayer graphene: a self consistent approach, arXiv e-prints, arXiv:1906.10570 (2019), arXiv:1906.10570 [cond-mat.str-el].